PERGAMON

Journal of the Mechanics and Physics of Solids
48 (2000) 1253–1283

JOURNAL OF THE
MECHANICS AND
PHYSICS OF SOLIDS

www.elsevier.com/locate/jmps

Isotropic constitutive models for metallic foams

V.S. Deshpande, N.A. Fleck*

Cambridge University Engineering Department, Trumpington Street, Cambridge CB2 1PZ, UK

Received 10 December 1998; received in revised form 9 August 1999

Abstract

The yield behaviour of two aluminium alloy foams (Alporas and Duocel) has been investigated for a range of axisymmetric compressive stress states. The initial yield surface has been measured, and the evolution of the yield surface has been explored for uniaxial and hydrostatic stress paths. It is found that the hydrostatic yield strength is of similar magnitude to the uniaxial yield strength. The yield surfaces are of quadratic shape in the stress space of mean stress versus effective stress, and evolve without corner formation. Two phenomenological isotropic constitutive models for the plastic behaviour are proposed. The first is based on a geometrically self-similar yield surface while the second is more complex and allows for a change in shape of the yield surface due to differential hardening along the hydrostatic and deviatoric axes. Good agreement is observed between the experimentally measured stress versus strain responses and the predictions of the models.

Keywords: Metallic foams; Yield surface; Constitutive law; Plasticity theory

1. Introduction

Over the past few years, low cost aluminium foams have been produced for a wide range of potential applications such as the cores of sandwich panels and

* Corresponding author. Tel.: +44-1223-332650; fax: +44-1223-332662.
E-mail address: nafl@eng.cam.ac.uk (N.A. Fleck).

0022-5096/00/$ - see front matter
PII: S0022-5096(99)00082-4

various automotive parts. A typical aim is to develop lightweight structures which are adequately stiff and strong yet absorb large amounts of energy. The successful implementation of metallic foams requires the development of design methods based on engineering constitutive laws. A major aim of the current study is to provide a simple but reliable constitutive description of the yield behaviour of metallic foams.

Early theoretical studies (Gibson and Ashby, 1997) suggest that the hydrostatic strength of an isotropic foam is governed by cell wall stretching and scales with the relative density $\bar{\rho}$, whereas the uniaxial strength is governed by cell wall bending and scales with $\bar{\rho}^{3/2}$. Thus, for a relative density of $\bar{\rho} = 0.1$, the hydrostatic strength of the perfect structure is about three times the uniaxial strength. These theoretical predictions neglect the effect of imperfections in the microstructure. Recently, the effect of morphological defects on the elastic and plastic properties of foams has been addressed by various authors (e.g. Silva et al., 1995; Kraynik et al., 1997; Grenestedt, 1998). The main findings of these and other studies have been reviewed by Chen et al. (1999). Chen et al. (1999) comprehensively studied the effect of various geometrical imperfections on the in-plane yielding behaviour of 2D cellular materials using a combination of analytical and finite element methods. They found that cell wall waviness significantly reduces the hydrostatic strength of the regular honeycomb structure. Similarly, random imperfections in the form of cell wall misalignments and fractured cell walls reduce the hydrostatic strength to the same level as the uniaxial strength. The effect of a random dispersion of cell size in a Γ- or δ-Voronoi structure is relatively small and the yield surfaces of these structures have approximately the same size and shape as those of ideal hexagonal honeycombs. Chen et al. (1999) predict nearly circular yield surfaces in the stress space of mean stress versus effective stress for honeycombs with either fractured cell walls or cell wall misalignments. Kraynik et al. (1997) found a similar sensitivity of hydrostatic strength to the presence of cell wall misalignments in open cell 3D elastic foams. These analyses demonstrate that a small degree of imperfections suffices to induce bending deformation in the cell walls under all macroscopic stress states.

Experimental data for the multi-axial yield of foamed metals are limited. The main contributions are those of Triantafillou et al. (1989) and Gioux et al. (2000). Triantafillou et al. (1989) conducted axisymmetric tests on an open-cell aluminium foam under combined axial tension and radial compression. Gioux et al. (2000) reported yield data for closed and open cell aluminium foams under a variety of biaxial, shear and axisymmetric loadings. The presence of experimental scatter in these studies has made it difficult to establish the shape of the yield surfaces. Moreover, only the initial yield surface has been addressed. In many design situations, for example in energy absorbing devices, an understanding of the post-yield behaviour is essential.

Miller (2000) has recently proposed a continuum plasticity framework for metallic foams. He modified the Drucker–Prager yield criterion and introduced three adjustable parameters to fit the yield surface to the then available experimental data; these data are the uniaxial tensile and compressive yield

strengths, and the ratio of radial to axial plastic strain rate in an axisymmetric test, i.e. the "plastic Poisson's ratio". He assumed an associated flow rule and based the hardening law upon the uniaxial compressive behaviour to give a complete constitutive representation of the plastic behaviour. In contrast, the constitutive model of Zhang et al. (1997, 1998) for polymer foams adopts a non-associated flow rule to account for the low observed values of plastic Poisson's ratio. Zhang et al. use a hardening rule based upon the plastic volumetric strain. For the case of metallic foams micromechanical arguments suggest that associated flow on the microscopic scale translates to the macroscopic scale, (Hill, 1967; Gurson, 1977) therefore, we anticipate that plastic normality is satisfied.

In this paper the yield surfaces of an open cell and a closed cell aluminium foam are measured for axisymmetric compressive stress states. The evolution of the yield surfaces under uniaxial and hydrostatic compression is explored. Two phenomenological isotropic constitutive models with different levels of complexity are then developed to model the observed behaviour.

2. Experimental investigation

The overall aim of the experimental program is to

1. determine the stress versus strain responses of Alporas and Duocel foams under proportional axisymmetric compressive loading, and
2. investigate the shape of the initial yield surface and its evolution under hydrostatic and uniaxial compressive loadings.

2.1. Materials

Two types of foams were investigated: Alporas and Duocel aluminium alloy foams. Alporas is a closed cell foam manufactured by the Shinko Wire Company, Amagasaki, Japan. The composition of the cell walls is Al–Ca 5–Ti 3 (wt.%). Two relative densities, $\bar{\rho} = 8.4\%$ and $\bar{\rho} = 16\%$ were considered; for both densities the average cell size is approximately 4 mm. In the following we shall refer to the Alporas foam of density $\bar{\rho} = 8.4\%$ as "low density Alporas foam" and the Alporas foam of density $\bar{\rho} = 16\%$ as "high density Alporas foam". The open-cell Duocel foam manufactured by ERG, Oakland, CA, USA, is made from Al6101–T6 alloy. We tested a foam of relative density $\bar{\rho} = 7.0\%$ and average cell size 2.5 mm. Further details on the structure, manufacturing processes and on the suppliers of these foams are given by Ashby et al. (1998). Andrews et al. (2000) reported that Alporas foam specimens with at least five cells along each leading dimension gave macroscopically representative measures of strength and elastic modulus. For the Duocel foam, specimens with at least seven cells in each direction were adequate. In this study, circular cylindrical specimens of diameter 30 mm and length 52 mm were cut to shape by spark machining to minimise

damage to the cell edges. With this choice of specimen dimensions, all the specimens have at least seven cells in each direction.

2.2. Apparatus

A high pressure triaxial system was used to measure the axisymmetric compressive stress–strain curves and to probe the yield surface. It consists of a pressure cell and a piston for the application of axial force. Hydraulic fluid is used as the pressurising medium. The triaxial cell is balanced so that application of hydraulic pressure produces hydrostatic loading on the specimen. Thus, a pressure p gives a compressive axial and radial stress of magnitude p. Further details are given by Akisanya et al. (1997). In order to superimpose an axial stress on top of the hydrostatic loading, the piston of the triaxial cell was displaced by a screw-driven test machine. The axial load was measured using a load cell internal to the triaxial cell, and the axial displacement was measured with a linear voltage displacement transducer (LVDT) on the test machine cross-head. The axial force and axial displacement were recorded using a computerised data logger and the oil pressure was recorded manually from a pressure gauge on the oil line.

The specimens were prepared for the triaxial tests by wrapping them in an aluminium shim (25 μm thick), encassing them in a rubber membrane and then sealing using a wedge arrangement as shown in Fig. 1. This elaborate arrangement was required in order to achieve satisfactory sealing at pressures in excess of 5 MPa.

3. Measurement protocol

The applied stresses are sketched in Fig. 2. p is the fluid pressure and σ is the applied compressive axial stress (both are taken to be positive in compression). The mean stress σ_m and the von Mises effective stress σ_e follow as,

$$\sigma_m = -\left(p + \frac{\sigma}{3}\right) \tag{1a}$$

and

$$\sigma_e = |\sigma| \tag{1b}$$

respectively. Note that the magnitude of the radial Cauchy stress on the specimen equals the fluid pressure p while the contribution σ to the axial Cauchy stress is evaluated from the applied axial force and the current cross-sectional area of the specimen. Unless otherwise stated, the strain rate in the triaxial tests coincides with an axial imposed strain rate of $4 \times 10^{-5}\ s^{-1}$.

3.1. Stress versus strain response

Three types of stress versus strain curves were measured, as follows.

1. Uniaxial compression tests

   Uniaxial compression tests were performed using a standard screw driven test machine. The load was measured by the load cell of the test machine and the machine platen displacement was used to define the axial strain in the specimen. The loading platens were lubricated with PTFE spray to reduce friction.

   In order to determine the plastic Poisson's ratio, the specimens were deformed in increments of approximately 5% axial plastic strain and the diameter was measured at three points along the length of the specimen using a micrometer. The plastic Poisson's ratio was defined as the negative ratio of the transverse logarithmic strain rate to the axial logarithmic strain rate.

2. Hydrostatic compression tests

   Hydrostatic tests were performed using the triaxial cell. The hydrostatic

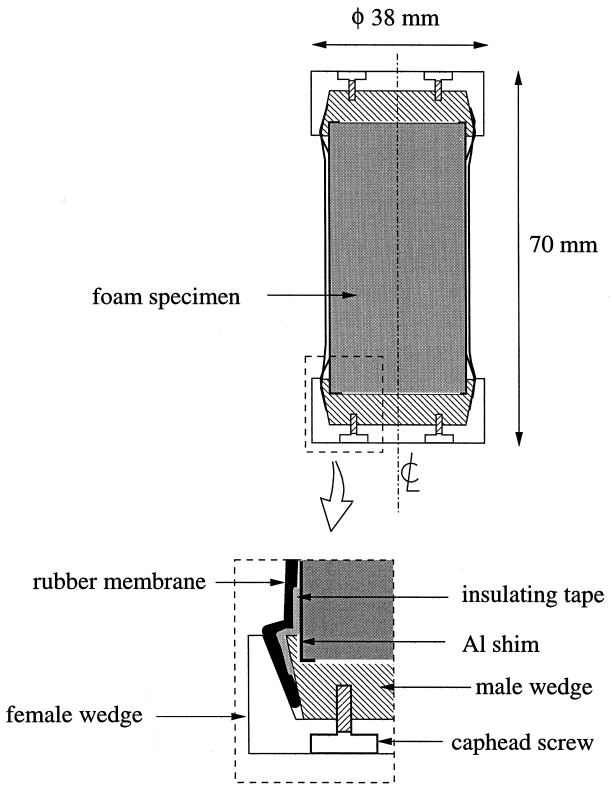

Fig. 1. Specimen assembly.

pressure was increased in increments of 0.1 MPa and the corresponding volumetric strain was deduced from the axial displacement. The volumetric strain was assumed to be three times the axial strain. A *posteri* checks of specimen deformation confirmed that the foams deform in an isotropic manner.

3. Proportional axisymmetric stress paths

The stress versus strain response along a number of proportional stress paths was measured. The direction of stressing is defined by the relation $\sigma_m = -\eta\sigma_e$, with the parameter η taking values over the range $\eta = 1/3$ (for uniaxial compression) to $\eta = \infty$ (for hydrostatic compression). In a typical proportional loading experiment, the hydrostatic pressure and the axial load were increased in small increments keeping η constant. The axial displacement was measured at each load increment and was used to define the axial strain.

3.2. Yield surface measurements

The initial yield surface was determined for the Alporas and Duocel foams by probing each specimen through the stress path sketched in Fig. 3, using the triaxial cell. First, the specimen was pressurised until the offset axial plastic strain was 0.3%, as indicated by the stress path 0→1 in Fig. 3. This pressure was taken

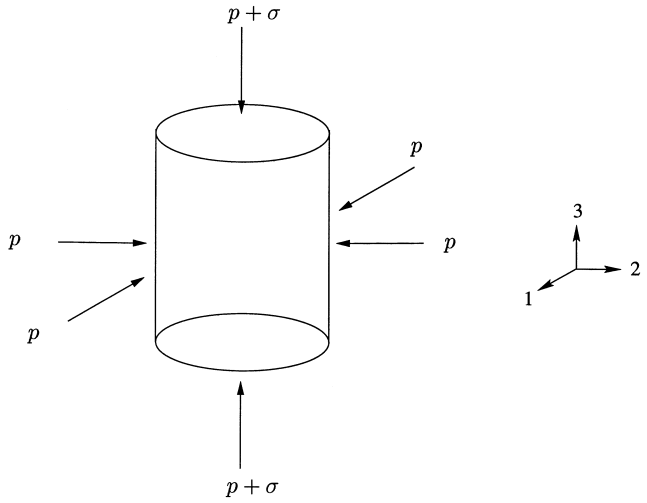

$$\text{mean stress,} \quad \sigma_m = -(p + \tfrac{1}{3}\sigma)$$

$$\text{effective stress,} \quad \sigma_e = |\sigma|$$

Fig. 2. Axisymmetric loading of specimen.

as the yield strength under hydrostatic loading. The pressure was then decreased by about 0.1 MPa along stress path 1→2, and an axial displacement rate of 2×10^{-3} mm s^{-1} (strain rate of 4×10^{-5} s^{-1}) was applied until the offset axial strain had incremented by 0.3%, referred to as path 2→3 in Fig. 3. The axial load was then removed (path 3→4) and the pressure was decreased further (path 4→5), and the procedure was repeated (path 5→6→7). This probing procedure was continued until the pressure p was reduced to zero; in this limit the stress state consisted of uniaxial compressive axial stress (path 0→8) and the measured uniaxial yield strength was found to be within a few percent of the uniaxial yield strength from a proportional uniaxial compression test. The locus of yield points, defined at 0.3% offset axial strain, was plotted in mean stress versus effective stress space.

Probing of the yield surface was also performed by starting at the uniaxial yield point and slowly building up the pressure; this alternative procedure gave no substantial difference in the yield surface shape and size indicating that the plastic strain accumulated during the probing process has a negligible effect on the measurements.

In order to measure the evolution of the yield surface under uniaxial loading, the initial yield surface was probed as described above. The specimen was then compressed uniaxially to a desired level of axial strain and the axial load was removed; the yield surface was then re-probed. By repetition of this technique, the evolution of the yield surface under uniaxial loading was measured at a number of levels of axial strain from a single specimen. The evolution of the yield surface under hydrostatic loading was measured in a similar manner.

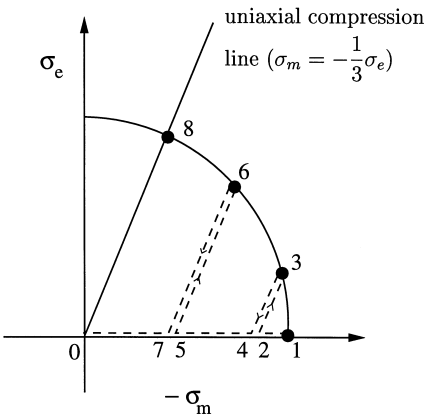

Fig. 3. Probing of the yield surface. In the example shown, the specimen is taken through the sequence of loading states 0, 1, 2, 3, 4, 5, 6, 7, 0, 8. The final loading segment 0→8 corresponds to uniaxial compression.

4. Experimental results

The uniaxial compressive responses of the Alporas and Duocel foams are shown in Fig. 4, using the axes of axial Cauchy stress and true (logarithmic) plastic axial strain. The plastic Poisson's ratio did not change with axial strain to within measurement accuracy and an average value was used to calculate the axial Cauchy stress.

Results from hydrostatic compression tests are included in Fig. 4. In this case we take as axes the pressure and the true (logarithmic) volumetric strain. A comparison between the hydrostatic and uniaxial compression stress versus strain curves shows that the hardening rate under hydrostatic compression is much greater than the hardening rate under uniaxial compression for the high density Alporas foam ($\bar{\rho} = 16\%$). In contrast, the hydrostatic and uniaxial hardening rates are comparable for the low density Alporas foam ($\bar{\rho} = 8.4\%$) and the Duocel foam ($\bar{\rho} = 7.0\%$). Repeated uniaxial and hydrostatic tests showed that the stress versus strain curves of Fig. 4 have a scatter of about $\pm 5\%$ in stress at any given value of strain. The initial stages of the hydrostatic and uniaxial compression curves for the three foams are shown in Fig. 5. We note that the magnitude of the hydrostatic yield strength is about 20% less than the uniaxial yield strength for each of the foams tested.

The initial yield surfaces for the three foams are plotted in Fig. 6, using the axes of mean stress and effective stress. Both the mean stress and effective stress values

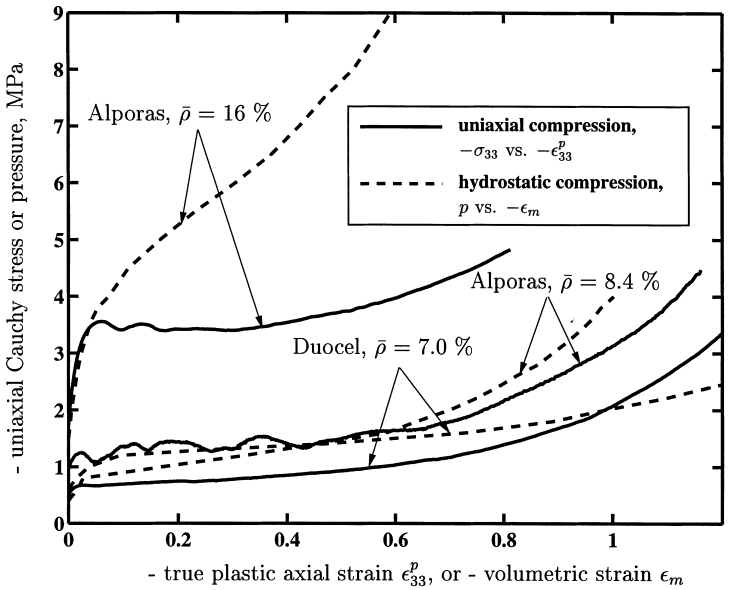

Fig. 4. Uniaxial and hydrostatic compression stress–strain curves for the low and high density Alporas, and Duocel foams.

have been normalised by the uniaxial yield strength of the respective specimen. The shapes of the yield surfaces are repeatable (at least five similar tests were conducted to check for scatter), and the data are adequately fitted by a quadratic function of mean stress and effective stress. The evolution of the yield surfaces under uniaxial and hydrostatic compressive loading is shown in Figs. 7–9 for the low density Alporas, high density Alporas and the Duocel foams, respectively. It is clear that the yield surfaces remain quadratic in shape and show no evidence of corner development at the loading point. Under uniaxial loading the yield surfaces evolve in approximately a geometrically self-similar manner (i.e. their shapes do not change), while under hydrostatic loading the yield surfaces elongate along the hydrostatic axes. For the case of the Duocel foam under hydrostatic loading no cross-hardening occurs: the shear yield strength remains unchanged with hydrostatic straining.

The early stage of yield surface evolution for the high density Alporas is shown in Fig. 10 for a primary loading path of uniaxial compression. Significant hardening occurs over an initial strain increment of 2%, but the rate of hardening then decreases as the plateau stress is approached.

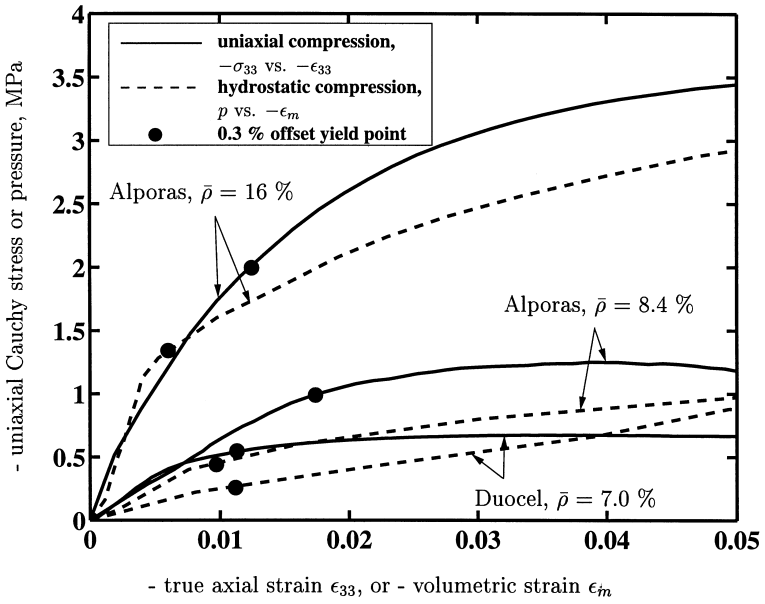

Fig. 5. Initial stages of the uniaxial and hydrostatic compression stress–strain curves for the low and high density Alporas, and Duocel foams.

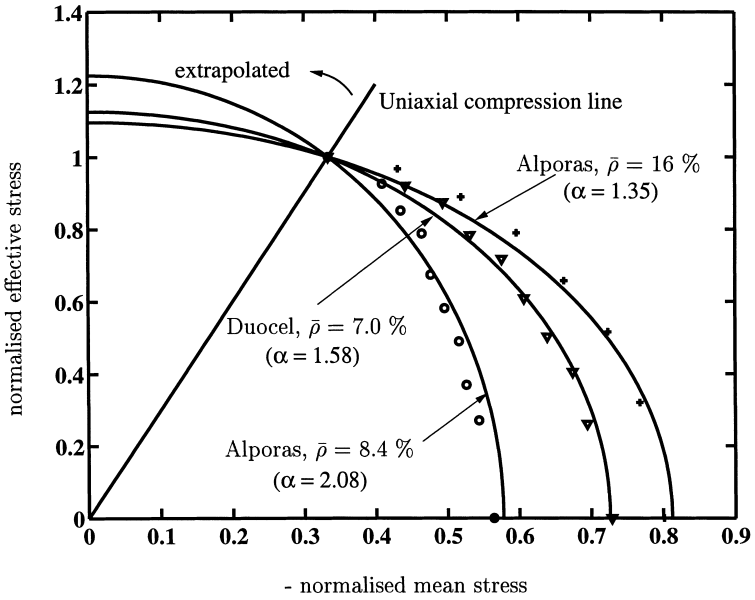

Fig. 6. Initial yield surfaces of the low and high density Alporas, and Duocel foams. The stresses have been normalised by the uniaxial yield strength (0.5 MPa for Duocel, 1.0 MPa for Alporas of $\bar{\rho} = 8.4\%$ and 2.0 MPa for Alporas of $\bar{\rho} = 16\%$).

5. Constitutive modelling

In this section two isotropic constitutive models are developed for metallic foams, based on the experimental observations described above. It is assumed that the yield function Φ depends only on the first two stress invariants σ_m and σ_e and is independent of the third stress invariant $J_3 = (\sigma'_{ij}\sigma'_{jk}\sigma'_{ki})^{1/3}$; here the prime denotes the deviatoric part of the stress tensor. We shall also assume that the yield function is even in σ_m. This is supported by recent experimental studies. Harte et al. (1999) found that the uniaxial tensile yield strength is approximately equal to the uniaxial compressive yield strength for both Alporas and Duocel foams: their data are reproduced in Fig. 11 along with the uniaxial compressive data from the present study. Gioux et al. (2000) measured the yield surface shapes of Alporas and Duocel foams and concluded that the asymmetry in shape with respect to mean stress is negligible.

5.1. Self-similar yield surface model

We define a yield function Φ by

$$\Phi \equiv \hat{\sigma} - Y \leq 0, \tag{2}$$

where the equivalent stress $\hat{\sigma}$ is given by

$$\hat{\sigma}^2 \equiv \frac{1}{\left[1+(\alpha/3)^2\right]}\left[\sigma_e^2 + \alpha^2\sigma_m^2\right]. \tag{3}$$

Here, σ_e is the von Mises effective stress $\sigma_e \equiv \sqrt{\frac{3}{2}\sigma'_{ij}\sigma'_{ij}}$, σ_m is the mean stress, $\sigma_m \equiv \sigma_{kk}/3$, and the parameter α defines the shape of the yield surface. Again, a prime denotes the deviatoric quantity.

Eqs. (2) and (3) together describe a yield surface of elliptical shape in (σ_m, σ_e) space, with the uniaxial yield strength in tension and compression equal to Y, and the hydrostatic yield strength equal to $\frac{\sqrt{1+(\alpha/3)^2}}{\alpha}Y$. Thus, the parameter α defines the aspect ratio of the ellipse; in the limit $\alpha = 0$, $\hat{\sigma}$ reduces to σ_e and the von Mises yield criterion is recovered. Fig. 6 shows that the yield surfaces defined by Eq. (2) fit the experimental data for the three foams very well provided the value of α is chosen appropriately.

The plastic strain rate $\dot{\epsilon}^p_{ij}$ is assumed to be normal to the yield surface (associated flow) and is given by

$$\dot{\epsilon}^p_{ij} = \frac{1}{H}\frac{\partial \Phi}{\partial \sigma_{ij}}\frac{\partial \Phi}{\partial \sigma_{kl}}\breve{\sigma}_{kl}, \tag{4}$$

where H is the hardening modulus and $\breve{\sigma}_{ij}$ is the Jaumann stress rate. The

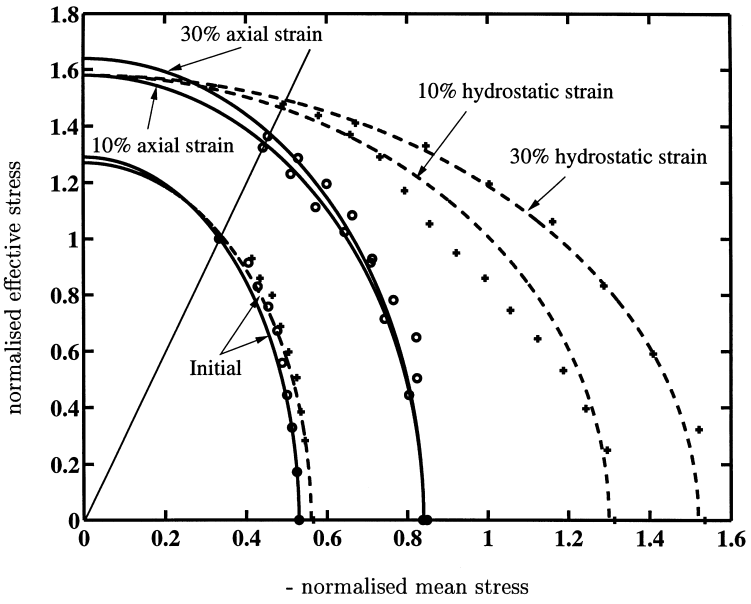

Fig. 7. Evolution of the yield surface of the low density Alporas foam under uniaxial and hydrostatic loading. The stresses have been normalised by the initial uniaxial yield strength = 1.0 MPa.

Jaumann rate has been used here to ensure objectivity to rigid body rotation. At temperatures well below the melting point of aluminium alloys, the deformation behaviour of the foams is almost rate independent and the hardening modulus H is chosen to be homogeneous and of degree zero in stress rate. In addition, H is chosen to evolve with a measure of the accumulated plastic strain $\hat{\epsilon}$ which will be made precise below. The plastic Poisson's ratio ν^p in a uniaxial compression test follows from Eqs. (2)–(4), and can be written explicitly in terms of the yield surface ellipticity α as

$$\nu^p = -\frac{\dot{\epsilon}^p_{11}}{\dot{\epsilon}^p_{33}} = \frac{(1/2) - (\alpha/3)^2}{1 + (\alpha/3)^2}. \tag{5}$$

The predicted dependence of ν^p upon α is shown in Fig. 12. Independently measured values of ν^p and of α (deduced from the measured ratio of hydrostatic to uniaxial strength) are included in the figure, for the three foams. Good agreement between these experimental measurements and predictions is seen in support of the assumption of associated flow. It is tentatively suggested that measurement of ν^p in a uniaxial compression test is a quick and simple method for establishing the value of α and thereby the shape of the yield surface including the hydrostatic strength. Experience suggests that the measurement of ν^p is best

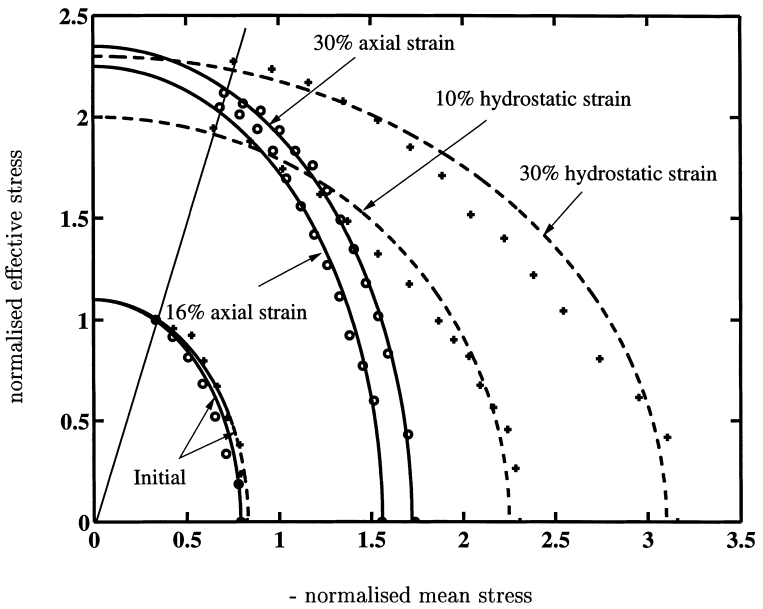

Fig. 8. Evolution of the yield surface of the high density Alporas foam under uniaxial and hydrostatic loading. The stresses have been normalised by the initial uniaxial yield strength = 2.0 MPa.

done by compressing a sample to a uniaxial strain of 20–30%, using suitably lubricated loading platens.

The expression (4) for the plastic strain rate can be simplified as follows. For continued plastic flow the consistency relation reads

$$\dot{\Phi} = 0 = \frac{\partial \Phi}{\partial \sigma_{ij}} \breve{\sigma}_{ij} + \frac{\partial \Phi}{\partial Y} \dot{Y}. \tag{6}$$

Upon noting from Eq. (3) that $\frac{\partial \Phi}{\partial Y} = -1$, the consistency relation reduces to

$$\frac{\partial \Phi}{\partial \sigma_{ij}} \breve{\sigma}_{ij} = \dot{Y}. \tag{7}$$

Now substitute Eq. (7) into the flow rule (4) to obtain

$$\dot{\epsilon}^{\mathrm{p}}_{ij} = \frac{\dot{Y}}{H} \frac{\partial \Phi}{\partial \sigma_{ij}}, \tag{8}$$

and introduce an equivalent strain rate $\dot{\hat{\epsilon}}$ which is the plastic work rate conjugate to $\hat{\sigma}$,

$$\hat{\sigma} \dot{\hat{\epsilon}} \equiv \sigma_{ij} \dot{\epsilon}^{\mathrm{p}}_{ij}. \tag{9}$$

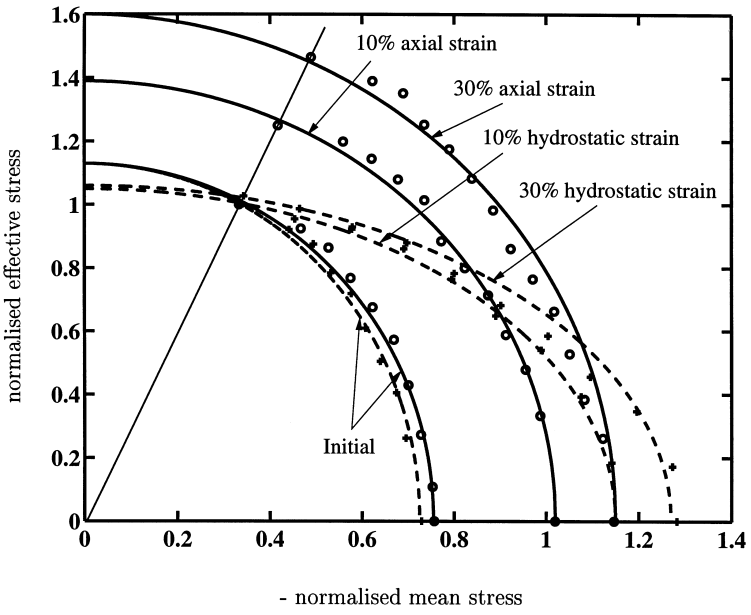

Fig. 9. Evolution of the yield surface of the Duocel foam under uniaxial and hydrostatic loading. The stresses have been normalised by the initial uniaxial yield strength = 0.5 MPa.

A straightforward connection can be obtained between $\dot{\hat{\epsilon}}$ and $\dot{Y}$ by substituting Eq. (8) into Eq. (9), and using the observation that Φ is homogeneous of degree 1 in $\boldsymbol{\sigma}$, to obtain

$$\dot{\hat{\epsilon}} = \frac{\dot{Y}}{H} = \frac{\dot{\hat{\sigma}}}{H}. \tag{10}$$

The flow rule (8) can now be re-written as

$$\dot{\epsilon}^{\mathrm{p}}_{ij} = \dot{\hat{\epsilon}} \frac{\partial \Phi}{\partial \sigma_{ij}}, \tag{11}$$

and the von Mises effective plastic strain rate $\dot{\epsilon}_{\mathrm{e}}$ and the volumetric plastic strain rate $\dot{\epsilon}_{\mathrm{m}}$ can be expressed as

$$\dot{\epsilon}_{\mathrm{e}} \equiv \sqrt{\frac{2}{3}\dot{\epsilon}'^{\mathrm{p}}_{ij}\dot{\epsilon}'^{\mathrm{p}}_{ij}} = \frac{\dot{\hat{\epsilon}}}{\left[1+(\alpha/3)^2\right]}\frac{\sigma_{\mathrm{e}}}{\hat{\sigma}}, \tag{12a}$$

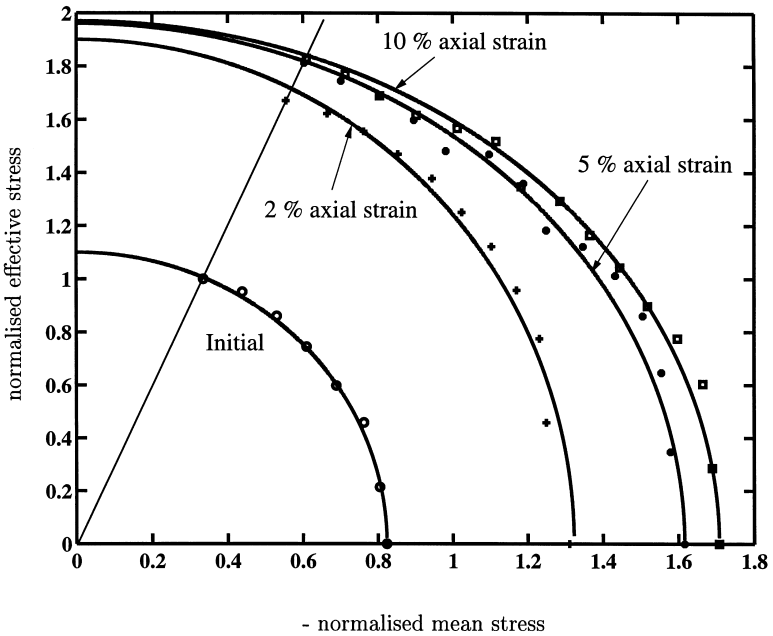

Fig. 10. Evolution of the yield surface of the high density Alporas foam under uniaxial loading. The stresses have been normalised by the initial uniaxial yield strength = 2.0 MPa.

and

$$\dot{\epsilon}_{\mathrm{m}} \equiv \dot{\epsilon}^{\mathrm{p}}_{kk} = \frac{\alpha^2 \dot{\hat{\epsilon}}}{\left[1 + (\alpha/3)^2\right]} \frac{\sigma_{\mathrm{m}}}{\hat{\sigma}}. \tag{12b}$$

Upon substituting the expressions for σ_{e} and σ_{m} from Eqs. (12a, b) into Eq. (3) and simplifying, we get an explicit expression for $\dot{\hat{\epsilon}}$ in terms of $\dot{\epsilon}_{\mathrm{e}}$ and $\dot{\epsilon}_{\mathrm{m}}$,

$$\dot{\hat{\epsilon}}^2 = \left[1 + \left(\frac{\alpha}{3}\right)^2\right]\left(\dot{\epsilon}_{\mathrm{e}}^2 + \frac{1}{\alpha^2}\dot{\epsilon}_{\mathrm{m}}^2\right). \tag{13}$$

To summarise, we have obtained explicit definitions for the equivalent stress $\hat{\sigma}$ and the work conjugate strain rate $\dot{\hat{\epsilon}}$. The plastic strain rate is given by the flow rule (11). It now remains to specify the hardening modulus H. In general, H is homogeneous and of degree zero in stress rate. Here we choose to restrict our definition of H to depend upon $\hat{\epsilon}$, and on the current direction of stress, $\boldsymbol{\sigma}/|\boldsymbol{\sigma}|$. The nature of this dependence is backed out approximately from the available experimental data as follows.

Recall that H is defined by the tangent modulus $H \equiv \dot{\hat{\sigma}}/\dot{\hat{\epsilon}}$ for a given stress state. In order to determine the dependence of H on stress path, consider a typical triaxial test wherein a foam is subjected to proportional stressing from zero. For

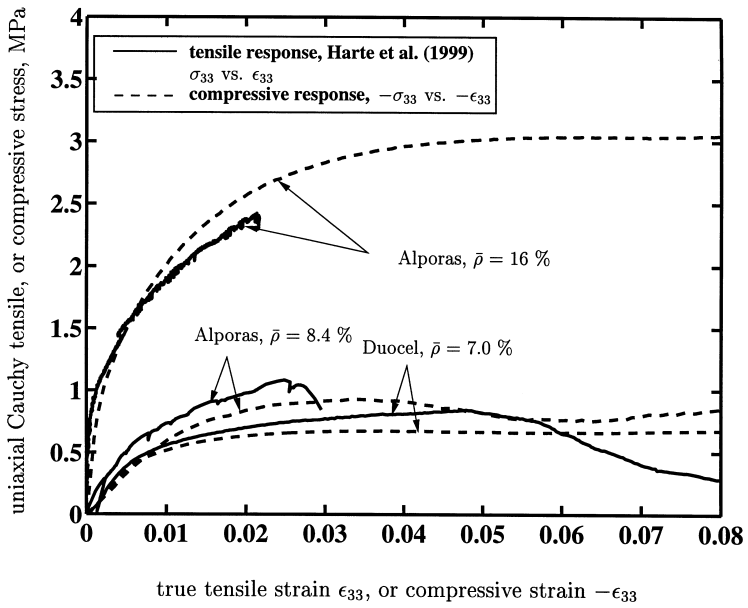

Fig. 11. Comparison between the uniaxial tensile and compressive responses of the low and high density Alporas, and Doucel foams.

this stress path, we calculate the increment $\Delta\hat{\sigma}$ corresponding to an increment in $\hat{\epsilon}$ from say 0 to 0.2 (i.e. $\Delta\hat{\epsilon} = 0.2$); the average tangent modulus over this increment is defined by

$$\bar{H} = \frac{\Delta\hat{\sigma}}{\Delta\hat{\epsilon}}. \tag{14}$$

This procedure was carried out for each foam by performing a series of proportional loading experiments, ranging from hydrostatic compression to uniaxial compression. The equivalent stress $\hat{\sigma}$ was calculated from the applied stresses p and σ using the definition (3) and an assumed value of α for the respective foam. The equivalent strain $\hat{\epsilon}$ is estimated from the plastic axial strain $\epsilon_{33}^{\mathrm{p}}$ using the relation

$$\hat{\epsilon} = \epsilon_{33}^{\mathrm{p}} \frac{\sqrt{\left(1+\alpha^2\eta^2\right)\left(1+(\alpha/3)^2\right)}}{1+\left(\alpha^2\eta/3\right)}, \tag{15}$$

for the proportional stress path $\eta \equiv |\sigma_{\mathrm{m}}/\sigma_{\mathrm{e}}|$. Note that Eq. (15) follows directly from the flow rule (11), and from the fact that the model gives proportional straining under proportional stressing.

The measured values of $\bar{H}$ are plotted against stress direction, parameterised by $\frac{\sigma_e}{\hat{\sigma}}\frac{1}{\sqrt{1+(\alpha/3)^2}}$ in Fig. 13. Here the numerical factor $\frac{1}{\sqrt{1+(\alpha/3)^2}}$ has been introduced so

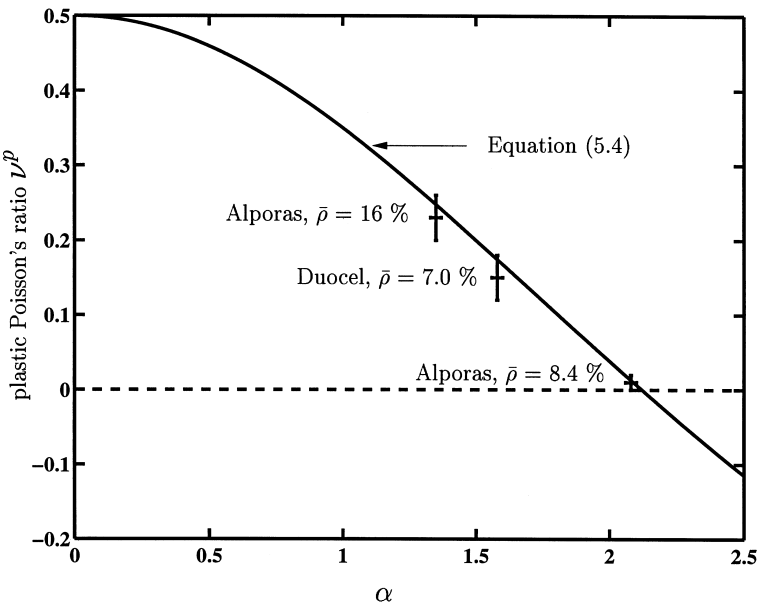

Fig. 12. Comparison between measured Poisson's ratio values and predictions assuming associated flow. The crosses denote the degree of uncertainty in experimental measurement.

that the stress parameter varies from zero to unity as we go from a purely hydrostatic stress state to a state of pure shear. The experimental data plotted in Fig. 13 reveal that the hardening modulus $\bar{H}$ varies linearly with $\sigma_e/\hat{\sigma}$. Therefore, we choose the tangent modulus H to obey the linear relation

$$H = \left[\frac{\sigma_e}{\hat{\sigma}} h_\sigma + \left(1 - \frac{\sigma_e}{\hat{\sigma}}\right) h_p\right], \tag{16}$$

where h_σ and h_p are the tangent moduli under uniaxial and hydrostatic compression, defined as follows.

Calibration of coefficients h_σ and h_p

Consider first the case of uniaxial compression; the material is subjected to a Cauchy stress σ_{33} and undergoes a logarithmic plastic strain ϵ^p_{33}. Then,

$$\hat{\sigma} = -\sigma_{33} \tag{17a}$$

and

$$\dot{\hat{\epsilon}} = -\dot{\epsilon}^p_{33}. \tag{17b}$$

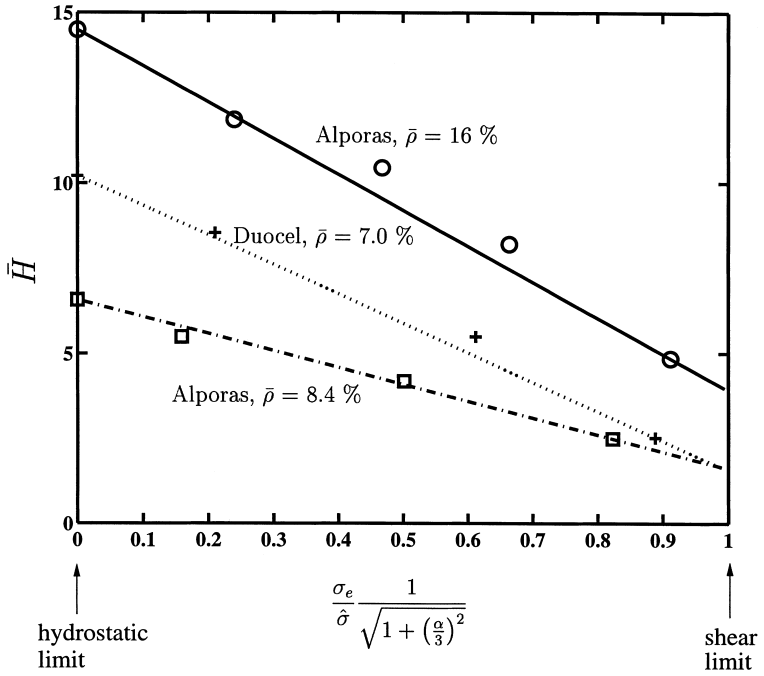

Fig. 13. Hardening modulus as a function of stress state for the low and high density Alporas, and Duocel foams.

The hardening modulus H for a uniaxial stress state reduces to $H = h_\sigma$ and so Eqs. (17a, b) provide the specification for h_σ,

$$h_\sigma(\hat{\epsilon}) = \frac{\dot{\sigma}_{33}}{\dot{\epsilon}^{\mathrm{p}}_{33}}. \tag{18}$$

Thus, the coefficient h_σ is the slope of the Cauchy stress versus logarithmic plastic strain curve in uniaxial compression at a strain level $\hat{\epsilon} = -\epsilon^{\mathrm{p}}_{33}$. Note that in the limiting case of a von Mises solid, we have $\alpha = 0$, $\hat{\sigma} = \sigma_{\mathrm{e}}$, and $\hat{\epsilon} = \epsilon_{\mathrm{e}}$. Then, Eq. (16) reduces to $H = h_\sigma$ and the Prandtl–Reuss J2 flow theory is recovered.

Second, consider hydrostatic compression. The equivalent stress $\hat{\sigma}$ is related to the hydrostatic pressure p via,

$$\hat{\sigma} = \frac{\alpha}{\sqrt{1 + (\alpha/3)^2}} p, \tag{19a}$$

and the equivalent strain rate is related to the volumetric strain rate $\dot{\epsilon}_{\mathrm{m}}$ by

$$\dot{\hat{\epsilon}} = -\frac{\sqrt{1 + (\alpha/3)^2}}{\alpha} \dot{\epsilon}_{\mathrm{m}}. \tag{19b}$$

Thus, we obtain via Eqs. (10) and (16),

$$h_p(\hat{\epsilon}) = \frac{-\alpha^2}{1 + (\alpha/3)^2} \frac{\dot{p}}{\dot{\epsilon}_{\mathrm{m}}}. \tag{20}$$

This relation provides the direct connection between $h_p(\hat{\epsilon})$ and the slope of the pressure versus logarithmic plastic volumetric strain curve in hydrostatic compression, at a strain level $\hat{\epsilon} = -\frac{\sqrt{1+(\alpha/3)^2}}{\alpha}\epsilon_{\mathrm{m}}$.

5.1.1. Simplified version of the self-similar model

A simplified version of the self-similar model is obtained by the choice

$$H\left(\hat{\epsilon}, \frac{\boldsymbol{\sigma}}{|\boldsymbol{\sigma}|}\right) \equiv h_\sigma(\hat{\epsilon}) \tag{21}$$

instead of Eq. (16). Thus, the hardening response is given directly by the uniaxial compression response. The remaining details of the model persist, with the plastic strain rate given by the flow rule (11). The simplified model predicts a stress versus strain relation for any stress path, including the hydrostatic limit, by taking the uniaxial hardening characteristic as the reference response.

Recall that for the case of uniaxial compression (or tension), the definitions of $\hat{\sigma}$ and $\dot{\hat{\epsilon}}$ have been normalised so that $\hat{\sigma}$ is the uniaxial stress and $\dot{\hat{\epsilon}}$ is the uniaxial plastic strain rate. Consequently, $H(\hat{\epsilon})$ equals the slope of the uniaxial Cauchy stress versus logarithmic plastic strain curve. This simplified self-similar model has

been implemented by Chen (1998) as a user-defined material constitutive law within the Finite Element code ABAQUS (HKS, 1997).

Gioux et al. (2000) have used this simplified model to fit their initial yield data for the low density Alporas and Duocel foams. Their data are well fitted by taking $\alpha \approx 1.4$ for both foams, in fair agreement with the values $\alpha = 2.08$ for the low density Alporas and $\alpha = 1.58$ for the Duocel foam, as measured in the current study. However, they observed lower values of strength for the low density Alporas than was measured in the present study. This is attributed to the fact that different batches of Alporas were used in the two studies, as discussed by Sugimura et al. (1998).

In the above model the yield surface evolves in a geometrically self-similar manner. However, this is not entirely consistent with experimental observations. A more sophisticated isotropic constitutive model is introduced below in order to account for the effect of stress path on the evolution of the yield surface shape.

5.2. Differential hardening model

A model is now developed such that the yield surface is not constrained to evolve in a geometrically self-similar manner. Specifically, the hydrostatic and shear yield strengths evolve independently and the model is thus termed "differential hardening". In similar manner to that described above, we define a quadratic yield surface of the form

$$\Phi \equiv \left(\frac{\sigma_e}{S}\right)^2 + \left(\frac{\sigma_m}{P}\right)^2 - 1 \le 0, \tag{22}$$

where S and P are now the yield strengths under deviatoric and hydrostatic loading, respectively. Associated flow (4) is again assumed. It remains to specify the hardening rule. The experiments of the present study show that the yield surface remains quadratic in shape with no evidence of corner development at the loading point. However, the yield surface does not evolve in a geometrically self-similar manner but elongates at different rates along the hydrostatic and deviatoric axes. This motivates us to define a hardening rule of the form

$$\begin{pmatrix} \dot{P} \\ \dot{S} \end{pmatrix} = \begin{pmatrix} h_{11} & h_{12} \\ h_{21} & h_{22} \end{pmatrix} \begin{pmatrix} \dot{\epsilon} \\ \dot{\gamma} \end{pmatrix}, \tag{23}$$

where the hardening matrix $(h_{\alpha\beta})$ and the kinematic quantities ϵ and γ remain to be specified. The kinematic variables ϵ and γ are defined to be work conjugates of P and S, respectively, i.e.

$$P\dot{\epsilon} + S\dot{\gamma} = \sigma_m \dot{\epsilon}_m + \sigma_e \dot{\epsilon}_e \equiv \sigma_{ij} \dot{\epsilon}^p_{ij}. \tag{24}$$

Therefore, we choose[1]

$$\dot{\epsilon} \equiv \frac{\sigma_{\mathrm{m}}}{P}\dot{\epsilon}_{\mathrm{m}} \tag{25a}$$

and

$$\dot{\gamma} \equiv \frac{\sigma_{\mathrm{e}}}{S}\dot{\epsilon}_{\mathrm{e}}. \tag{25b}$$

The hardening modulus H is related to the coefficients $h_{\alpha\beta}$ through the consistency relation

$$\dot{\Phi} = 0 = \frac{\partial \Phi}{\partial \sigma_{kl}}\breve{\sigma}_{kl} + \frac{\partial \Phi}{\partial S}\dot{S} + \frac{\partial \Phi}{\partial P}\dot{P} \tag{26}$$

as follows. Upon substituting the kinematic relations (25a, b) into the hardening rule (23) we have

$$\dot{P} = h_{11}\frac{\sigma_{\mathrm{m}}}{P}\dot{\epsilon}_{\mathrm{m}} + h_{12}\frac{\sigma_{\mathrm{e}}}{S}\dot{\epsilon}_{\mathrm{e}}, \tag{27a}$$

$$\dot{S} = h_{21}\frac{\sigma_{\mathrm{m}}}{P}\dot{\epsilon}_{\mathrm{m}} + h_{22}\frac{\sigma_{\mathrm{e}}}{S}\dot{\epsilon}_{\mathrm{e}}. \tag{27b}$$

The flow rule (4) gives the strain rates $\dot{\epsilon}_{\mathrm{m}}$ and $\dot{\epsilon}_{\mathrm{e}}$ in terms of the stress rates as

$$\dot{\epsilon}_{\mathrm{m}} = \frac{4\sigma_{\mathrm{m}}}{H\,P^2}\left(\frac{\sigma_{\mathrm{e}}\dot{\sigma}_{\mathrm{e}}}{S^2} + \frac{\sigma_{\mathrm{m}}\dot{\sigma}_{\mathrm{m}}}{P^2}\right), \tag{28a}$$

$$\dot{\epsilon}_{\mathrm{e}} = \frac{4\sigma_{\mathrm{e}}}{H\,S^2}\left(\frac{\sigma_{\mathrm{e}}\dot{\sigma}_{\mathrm{e}}}{S^2} + \frac{\sigma_{\mathrm{m}}\dot{\sigma}_{\mathrm{m}}}{P^2}\right). \tag{28b}$$

Now substitute Eqs. (27a, b) and (28a, b) into the consistency relation (26) and rearrange to obtain

[1] We have also considered a constitutive model in which (P, S) evolves with $(\epsilon_{\mathrm{m}}, \epsilon_{\mathrm{e}})$. The present scheme using the work conjugates (ϵ, γ) of (P, S) was found to give better agreement with the available experimental data.

$$\frac{2\sigma_m\dot{\sigma}_m}{P^2}\left[1-\frac{\sigma_e^2}{S^3}\left(h_{21}\frac{4\sigma_m^2}{H\,P^3}+h_{22}\frac{4\sigma_e^2}{H\,S^3}\right)-\frac{\sigma_m^2}{P^3}\left(h_{11}\frac{4\sigma_m^2}{H\,P^3}+h_{12}\frac{4\sigma_e^2}{H\,S^3}\right)\right]$$
$$+\frac{2\sigma_e\dot{\sigma}_e}{S^2}\left[1-\frac{\sigma_e^2}{S^3}\left(h_{21}\frac{4\sigma_m^2}{H\,P^3}+h_{22}\frac{4\sigma_e^2}{H\,S^3}\right)-\frac{\sigma_m^2}{P^3}\left(h_{11}\frac{4\sigma_m^2}{H\,P^3}+h_{12}\frac{4\sigma_e^2}{H\,S^3}\right)\right]$$
$$=0. \tag{29}$$

Thus, the expression inside each of the square brackets equals zero, and H is stipulated by

$$H\equiv\frac{4}{P}\left(\frac{\sigma_m}{P}\right)^2\left[\frac{h_{11}}{P}\left(\frac{\sigma_m}{P}\right)^2+\frac{h_{12}}{S}\left(\frac{\sigma_e}{S}\right)^2\right]$$
$$+\frac{4}{S}\left(\frac{\sigma_e}{S}\right)^2\left[\frac{h_{21}}{P}\left(\frac{\sigma_m}{P}\right)^2+\frac{h_{22}}{S}\left(\frac{\sigma_e}{S}\right)^2\right]. \tag{30}$$

Calibration of the hardening terms $h_{\alpha\beta}$

In this section we shall first make precise the definitions of the coefficients $h_{\alpha\beta}$ and then discuss the methodology used to calibrate them against the available experimental data.

Under a hydrostatic stress σ_m, the volumetric plastic strain rate is given by

$$\dot{\epsilon}_m=\frac{4\sigma_m}{H\,P^2}\left(\frac{\sigma_m\dot{\sigma}_m}{P^2}\right), \tag{31}$$

where the hardening rate H follows from Eq. (30) as

$$H=\frac{4h_{11}}{P^6}\sigma_m^4. \tag{32}$$

Upon noting that $\sigma_m=-P$ under a hydrostatic compressive stress σ_m, Eqs. (31) and (32) reduce to

$$h_{11}=\frac{\dot{\sigma}_m}{\dot{\epsilon}_m}. \tag{33}$$

Thus, h_{11} is the slope of the pressure versus the plastic part of the logarithmic volumetric strain curve at any given stage of deformation. The hardening rule (23) permits the shear yield strength S to evolve under hydrostatic straining according to

$$\dot{S}=h_{21}\dot{\epsilon}_m. \tag{34}$$

Therefore, h_{21} is the slope of the shear yield strength versus the plastic part of the logarithmic volumetric strain curve.

A similar analysis for shear straining gives

$$h_{22} = \frac{\dot{\sigma}_e}{\dot{\epsilon}_e}, \tag{35a}$$

and

$$h_{12} = \frac{\dot{P}}{\dot{\epsilon}_e}. \tag{35b}$$

Thus, h_{22} is the slope of the effective stress versus the plastic part of the logarithmic effective strain curve, and h_{12} is the slope of the hydrostatic strength versus the plastic part of the logarithmic effective strain curve.

Next, we outline the methodology used in the present study to calibrate $h_{\alpha\beta}$ against the available experimental data. Motivated by Eqs. (33) and (34) we assume that h_{11} and h_{21} depend only on ϵ, as defined in Eq. (25a). Thus, $h_{11}(\epsilon)$ follows directly from Eq. (33) and the hydrostatic compression stress versus strain curve. h_{21} is determined from the yield surface evolution under hydrostatic compression, that is

$$\begin{pmatrix} \Delta P \\ \Delta S \end{pmatrix} = \begin{pmatrix} h_{11} & h_{12} \\ h_{21} & h_{22} \end{pmatrix} \begin{pmatrix} \Delta\epsilon_m \\ 0 \end{pmatrix}, \tag{36}$$

where Δ is a finite increment. This gives,

$$\frac{h_{21}}{h_{11}} = \frac{\Delta S}{\Delta P}. \tag{37}$$

For the three foams tested in this study, the ratio h_{21}/h_{11} was observed to be approximately constant, i.e. independent of the level of plastic strain. Thus, for simplicity it is assumed that h_{21} is a fixed fraction of h_{11} and given by

$$h_{21} = \alpha_{21} h_{11}. \tag{38}$$

For example, $\alpha_{21} \approx 0.4$ for the low density Alporas; this is calculated from Fig. 7 for strain increments $\Delta\epsilon_m = 0.1$ and 0.3.

It now remains to calibrate h_{22} and h_{12}. In analogous fashion to that described for h_{11} and h_{21}, we assume that h_{22} and h_{12} depend only on γ and that h_{12} is a constant fraction α_{12} of h_{22},

$$h_{12} = \alpha_{12} h_{22}. \tag{39}$$

In the present study shear tests were not conducted. Thus, the coefficient h_{22} could not be calculated in a direct fashion. Instead, h_{22} was deduced from the uniaxial and hydrostatic compression stress versus strain data as explained below.

Under a uniaxial compressive stress σ_{33}, the axial strain rate $\dot{\epsilon}_{33}^p$ follows from

the flow rule as

$$\dot{\epsilon}^{\mathrm{p}}_{33} = \frac{4\sigma^2_{33}}{H}\left(\frac{1}{S^2}+\frac{1}{9P^2}\right)^2 \dot{\sigma}_{33}, \tag{40}$$

where

$$H = \frac{4}{P}\left(\frac{\sigma_{33}}{3P}\right)^2\left[\frac{h_{11}}{P}\left(\frac{\sigma_{33}}{3P}\right)^2+\frac{h_{12}}{S}\left(\frac{\sigma_{33}}{S}\right)^2\right] + \frac{4}{S}\left(\frac{\sigma_{33}}{S}\right)^2\left[\frac{h_{21}}{P}\left(\frac{\sigma_{33}}{3P}\right)^2+\frac{h_{22}}{S}\left(\frac{\sigma_{33}}{S}\right)^2\right], \tag{41}$$

from Eq. (30). Now take $h_{12} = \alpha_{12}h_{22}$ and $h_{21} = \alpha_{21}h_{11}$, and re-arrange Eq. (40) to get

$$h_{22}(\gamma) = \frac{\dot{\sigma}_{33}\left(\frac{1}{S^2}+\frac{1}{9P^2}\right)^3}{\dot{\epsilon}^{\mathrm{p}}_{33}\left(\frac{\alpha_{12}}{9S^3P^3}+\frac{1}{S^6}\right)} - \frac{\left(\frac{1}{81P^6}+\frac{\alpha_{21}}{9P^3S^3}\right)h_{11}(\epsilon)}{\left(\frac{\alpha_{12}}{9S^3P^3}+\frac{1}{S^6}\right)}, \tag{42}$$

where $\gamma \equiv -\int(\sigma_{33}/S)\,\mathrm{d}\epsilon_{\mathrm{e}}$ and $\epsilon \equiv \int(\sigma_{33}/3P)\,\mathrm{d}\epsilon_{\mathrm{m}}$. Thus, Eq. (42) gives h_{22} in terms of the parameters h_{11}, α_{12} and α_{21}, with α_{12} as an unknown. The ratio, α_{12} is obtained from an iterative process as explained below. For a starting value of α_{12}, h_{22} is calculated from Eq. (42) and the differential hardening model is used to predict the stress versus strain response for a proportional stress path specified by $\sigma_{\mathrm{m}} = -\eta\sigma_{\mathrm{e}}$, where $1/3 < \eta < \infty$ (in the present study we take the case $\eta = 3.0$). The predicted stress versus strain response is compared with the measured stress versus strain curve and the above procedure is repeated with different values of α_{12} until good agreement between the model and the experimental data is obtained. The value of α_{12} that gives the best fit between the model and the experimental data is taken as the correct value of α_{12}.

The plastic part of the constitutive law has now been fully specified. In order to complete the constitutive description for the two models given above we assume isotropic elastic behaviour, such that the elastic strain rate $\dot{\epsilon}^{\mathrm{e}}_{ij}$ is given by

$$\dot{\epsilon}^{\mathrm{e}}_{ij} = \frac{1+\nu^{\mathrm{e}}}{E}\breve{\sigma}_{ij} - \frac{\nu^{\mathrm{e}}}{E}\dot{\sigma}_{kk}\delta_{ij}, \tag{43}$$

in terms of fixed values for the Young's modulus E and the elastic Poisson's ratio ν^{e}.

5.2.1. Relationship between the differential hardening model and the self-similar hardening model

With additional assumptions, the differential hardening model can be collapsed

to the simplified self-similar model (Section 5.1.1), but not to the full self-similar model (Section 5.1).

Consider first the reduction of the differential hardening model to the simplified self-similar model. The yield surface (22) of the differential hardening model reduces to the yield surface (2) of the self-similar model if S and P are constrained by the relations

$$S = \alpha P \tag{44a}$$

and

$$P = \frac{Y}{\alpha}\sqrt{1 + \left(\frac{\alpha}{3}\right)^2}. \tag{44b}$$

The hardening behaviours of the differential hardening and the simplified self-similar models co-incide if the hardening matrix $h_{\alpha\beta}$ in the differential hardening model is chosen to be

$$h_{\alpha\beta} = \left[1 + \left(\frac{\alpha}{3}\right)^2\right] h_\sigma \begin{pmatrix} 1/\alpha^2 & 1/\alpha \\ 1/\alpha & 1 \end{pmatrix}. \tag{45}$$

Thus, the differential hardening model can be made to reduce to the simplified self-similar model (Section 5.1.1) upon adopting the relations (44a, b) and (45).

Next, we attempt to reduce the differential hardening model to the full self-similar model (Section 5.1). Again, we constrain the yield surface in the differential hardening model to be an ellipse of fixed aspect ratio, as specified by Eqs. (44a, b). Then, we calibrate the hardening moduli $h_{\alpha\beta}$ of the differential hardening model so that the uniaxial and hydrostatic hardening responses are identical to those specified by relations (18) and (20), respectively of the full self-similar model. Consequently, the differential hardening model gives the same form of the flow rule (8) as specified by the full self-similar model, but with the hardening modulus $H(\boldsymbol{\sigma})$ now given by

$$H = \left[\left(\frac{\sigma_e}{\hat{\sigma}}\right)^2 h_\sigma + \left(1 - \left(\frac{\sigma_e}{\hat{\sigma}}\right)^2\right) h_p\right]. \tag{46}$$

Thus, with the yield surfaces constrained to evolve in a geometrically self-similar manner the differential hardening model predicts a quadratic dependence of hardening on the stress direction (parameterised by $\sigma_e/\hat{\sigma}$ in this case). In contrast, we choose to use a linear variation of hardening with stress direction in the full self-similar model as it gives the best agreement with the experimental data (see Fig. 13).

6. Comparison between the models and axisymmetric compression experiments

The stress versus strain response predictions of the models described above are now compared with experimental measurements for the Alporas and Duocel foams.

6.1. The self-similar model

Comparisons between the predictions of the self-similar model and experimental data are shown in Figs. 14–16 for the low density Alporas, high density Alporas and Duocel foams, respectively. In each figure, the equivalent stress $\hat{\sigma}$ is plotted against the equivalent strain $\hat{\epsilon}$ for proportional stress paths ranging from uniaxial compression to hydrostatic compression. The measured $\hat{\sigma}$ versus $\hat{\epsilon}$ responses have been calculated using the definition (3) for $\hat{\sigma}$ and the derived result (15) for $\hat{\epsilon}$. The hardening modulus of the self-similar yield surface model is calibrated against the uniaxial and hydrostatic compression data as stated by relation (16). Hence, the predictions of the model agree exactly with the uniaxial and hydrostatic compression data. To judge the accuracy of the model, predictions are compared with measured stress versus strain responses for intermediate values of η. The predictions of the self-similar model for the Alporas foams agree well with the

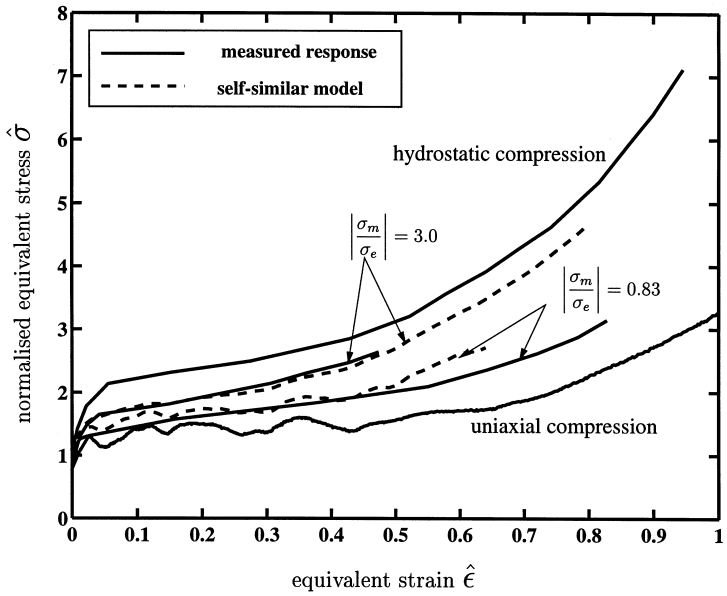

Fig. 14. Comparison between the measured equivalent stress vs. equivalent strain curves and predictions of the self-similar model for the low density Alporas foam. The equivalent stress has been normalised by the uniaxial yield strength = 1.0 MPa.

experimental observations, as shown in Figs. 14 and 15. By comparison the model overestimates the hardening modulus for the Duocel foam at $\hat{\epsilon} > 0.3$, see Fig. 16.

The simplified self-similar model, in which the hardening modulus is calibrated against uniaxial compression data only, makes the assumption that the foams have a unique equivalent stress $\hat{\sigma}$ versus equivalent strain $\hat{\epsilon}$ curve, as given by the uniaxial compressive response. Figs. 14–16 show that the measured stress versus strain responses do not collapse onto a single curve when plotted as $\hat{\sigma}$ versus $\hat{\epsilon}$. In particular, the simplified model underestimates the observed hardening behaviour for stress paths close to hydrostatic compression. These errors are greatest for the high density Alporas, as shown in Fig. 15. It should be noted here that the above conclusions remain valid if comparisons of the stress versus strain curves are made through axial stress and strain measures rather than the equivalent quantities.

6.2. Differential hardening model

The differential hardening model, Eqs. (22)–(42), takes as input the uniaxial and hydrostatic compressive responses, and the cross-hardening parameters α_{21} and α_{12}. The cross-hardening coefficient α_{21} is calculated from the hydrostatic yield surface evolution as detailed in Section 5.2 and is found to be $\alpha_{21} = 0.40$, 0.55 and 0.50 for the low density Alporas, high density Alporas and Duocel foams, respectively. The value $\alpha_{12} = 0$ is chosen to obtain the closest agreement between

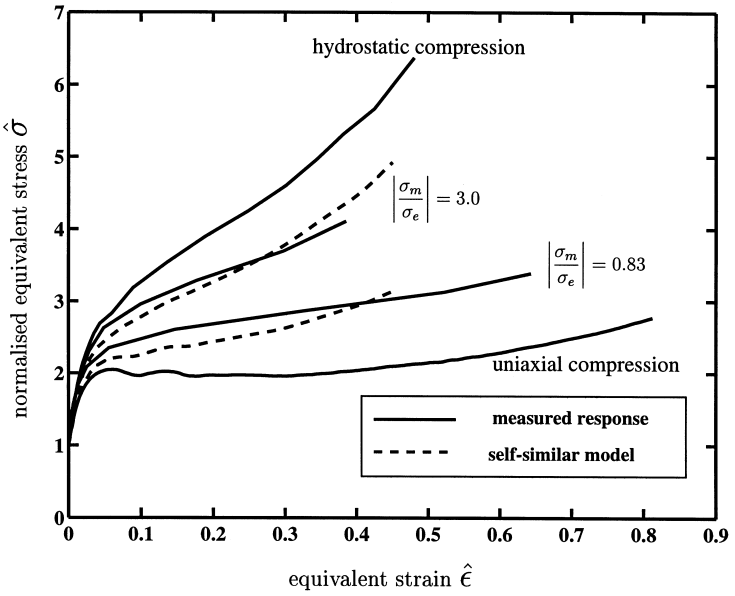

Fig. 15. Comparison between the measured equivalent stress vs. equivalent strain curves and predictions of the self-similar model for the high density Alporas foam. The equivalent stress has been normalised by the uniaxial yield strength = 2.0 MPa.

the differential hardening model and available experimental data for all three foams. This choice implies no cross-hardening between deviatoric straining and hydrostatic strength.

Recall that the differential hardening model is calibrated against uniaxial and hydrostatic compression data, and so the model agrees with the observed response for these loading paths. The predictions of this model are plotted in Fig. 17 for an intermediate proportional loading path, $\eta \equiv |\sigma_m/\sigma_e| = 3.0$, along with the corresponding experimental curves for the three foams and the corresponding predictions of the self-similar model. We note that the predictions of the differential hardening model are more accurate than those of the self-similar model. Similar comparisons of the two models have been made for other stress paths. Although these comparisons are not included (for the sake of brevity), they again indicate good agreement between the two models and the experimental data for the Alporas foams, and superior accuracy of the differential hardening model over the self-similar model for the Duocel foam.

7. Predictions for tensile and shear loading

In this section the predictions of the two models are compared with experimental data for the three foams under shear and tensile loading. These data

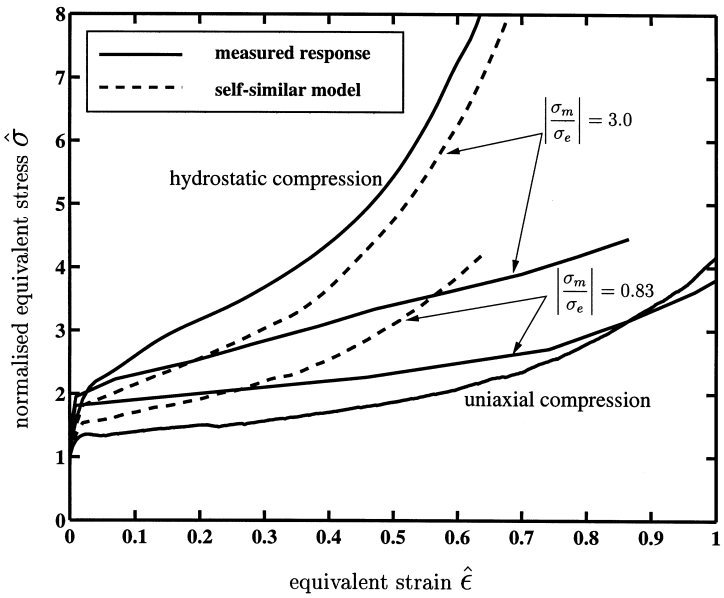

Fig. 16. Comparison between the measured equivalent stress vs. equivalent strain curves and predictions of the self-similar model for the Duocel foam. The equivalent stress has been normalised by the uniaxial yield strength = 0.5 MPa.

were obtained from studies by Harte et al. (1999) and Harte (1998) for tensile and shear loading, respectively.

7.1. Tensile response

A comparison between the experimentally observed tensile and compressive responses of the three foams is shown in Fig. 11. Both the self-similar model and the differential hardening model predict a tensile response identical to the measured uniaxial compressive response. The tensile experimental data are in close agreement with the compressive data until a peak tensile stress is attained at about 2.5%, 2.0% and 5.0% true tensile strain for the low density Alporas, high density Alporas and Duocel foams, respectively, see Fig. 11. This is followed by a softening response and subsequent fracture by tensile tearing. We conclude that both the self-similar and differential hardening models are accurate for prediction of the uniaxial tensile response up to the point of maximum tensile strength.

7.2. Shear response

The predictions of the two models for the shear response of the high density Alporas foam are plotted in Fig. 18 along with experimental data. The measured

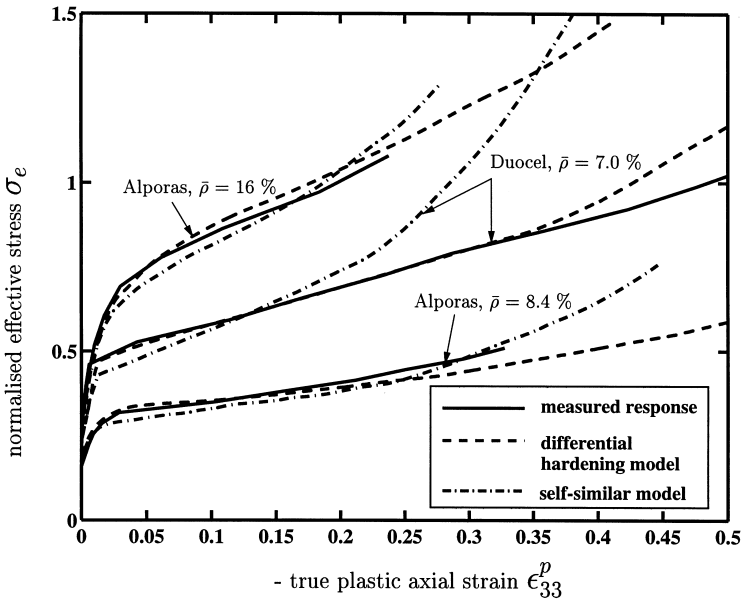

Fig. 17. Comparison between measured stress vs. strain curves and predictions using the differential hardening and self-similar models for a stress ratio $\eta \equiv |\sigma_m/\sigma_e| = 3.0$. The effective stress has been normalised by the uniaxial yield strength.

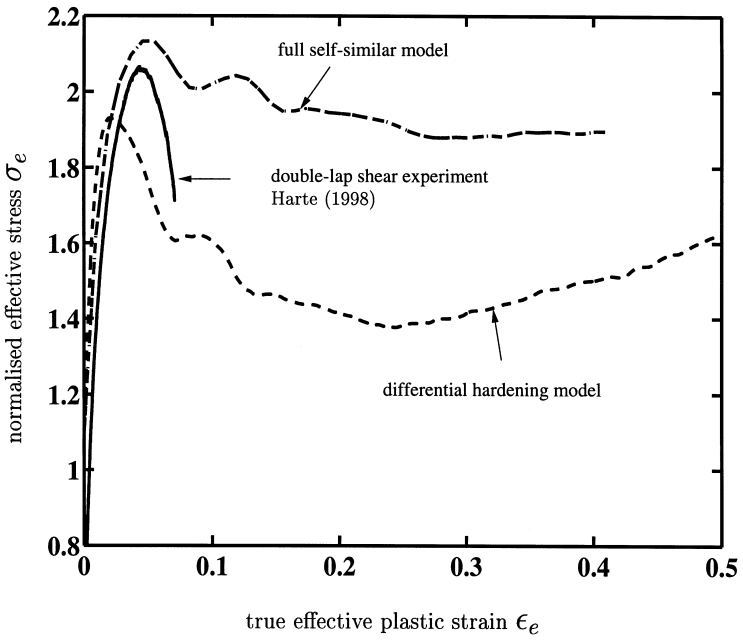

Fig. 18. Comparison between measured and predicted shear response of the high density Alporas foam. The effective stress has been normalised by the uniaxial yield strength = 2.0 MPa.

shear response of the high density Alporas was obtained by Harte (1998) using a double lap shear test. The measured response comprises an initial stable hardening behaviour, a peak in shear stress at an effective strain level $\epsilon_e \approx 0.05$, (engineering shear strain = $\sqrt{3}\epsilon_e$) and a subsequent softening behaviour associated with the formation of a macroscopic crack along the mid-plane of the specimen. The peak values of stress according to the two models are in satisfactory agreement with the observed strength of the high density Alporas foam. We note in passing that the simplified self-similar model gives almost identical predictions to the full self-similar model for a stress path of pure deviatoric loading.

8. Concluding remarks

The axisymmetric compressive stress versus strain responses have been measured for three aluminium alloy foams — low and high density Alporas, and Duocel. The initial yield surfaces and the evolution of the initial yield surfaces under uniaxial and hydrostatic compression have been investigated. We find that the yield surfaces are of quadratic shape in the stress space of mean stress versus effective stress, with the hydrostatic yield strength comparable to the uniaxial yield strength. Recently, Chen et al. (1999) have shown that microstructural

imperfections such as cell wall misalignments, missing cell edges and cell wall waviness induce bending deformation in the cell edges of 2D honeycombs under all imposed macroscopic stress states. The resulting yield surfaces in mean stress versus effective stress space resemble those of the current study. Next, consider the measured strain hardening response. As the yield surfaces evolve with plastic strain they remain quadratic in shape, with no evidence of corner development. Under uniaxial compression they evolve in approximately a geometrically self-similar manner while under hydrostatic compression they elongate along the hydrostatic axis. The three foams tested consistently show greater hardening under hydrostatic compression than under uniaxial compression.

Two phenomenological isotropic models for the yield behaviour are proposed herein. The experimental observations support the assumption of associated flow for both models. In the first model the yield surface is constrained to evolve in a geometrically self-similar manner, and the hardening law is calibrated against hydrostatic and uniaxial compression data. This model predicts the stress versus strain response of the foams under proportional loading conditions to reasonable accuracy. The more sophisticated differential hardening model permits an evolution of the shape of the yield surface. For proportional loading paths, the differential hardening model predicts the stress versus strain response of the three foams to a high level of accuracy. However, the added complexity of this model may make its use unwarranted and the simpler geometrically self-similar model suffices for most practical purposes.

The isotropic models presented here are adequate for proportional stress paths. For non-proportional stressing, the development of anisotropy may become important and alternative hardening models may then be needed. Indeed, preliminary investigations indicate that metallic foams develop anisotropy under large plastic strains. For example, when a sample of the high density Alporas is compressed uniaxially to a logarithmic axial strain of 0.70, the subsequent transverse strength is found to be about twice the current axial strength (Deshpande and Fleck, 1999). Isotropically hardening constitutive models are unable to account for the development of such anisotropy. Kinematic hardening models are required, and are suggested as a topic for future study.

Acknowledgements

The authors are grateful to DARPA/ONR for their financial support through MURI grant number N00014-1-96-1028 on the Ultralight Metal Structures Project at Harvard University. The authors would like to thank Professors M.F. Ashby, A.G. Evans, L.J. Gibson, J.W. Hutchinson and R.E. Miller for helpful discussions and S. Marshall, A. Heaver and I. Sridhar for help with the experimentation. The authors also thank Dr A.-M. Harte for providing the tensile and shear experimental data.

References

Akisanya, A.R., Cocks, A.C.F., Fleck, N.A., 1997. The yield behaviour of metal powders. International Journal of Mechanical Sciences 39 (12), 1315.

Andrews, E.W., Gioux, G., Onck, P., Gibson, L.J., 2000. The role of specimen size, specimen shape and surface preparation in mechanical testing of aluminium foams. Material Science and Engineering A, in press.

Ashby, M.F., Evans, A.G., Hutchinson, J.W., Fleck, N.A., 1998. Metal foams: a design guide. Technical Report CUED/C-MICROMECH/TR.3. Engineering Department, Cambridge University.

Chen, C., 1998. Manual for a UMAT user subroutine. Technical Report CUED/C-MICROMECH/TR.4. Department of Engineering, University of Cambridge.

Chen, C., Lu, T.J., Fleck, N.A., 1999. Effect of imperfections on the yielding of two-dimensional foams. Journal of Mechanics and Physics of Solids 47(11), 2235.

Deshpande, V.S., Fleck, N.A. 1999. Multi-axial yield of aluminium alloy foams. In: Banhart, J., Fleck, N.A., Ashby, M.F. (Eds.), MetFoam'99 Proceedings. Fraunhofer Institute, Bremen, Germany.

Gibson, L.J., Ashby, M.F., 1997. Cellular Solids: Structure and Properties, 2nd ed. Cambridge University Press, Cambridge.

Gioux, G., McCormack, T.M., Gibson, L.J., 2000. Failure of aluminium foams under multiaxial loads. International Journal of Mechanical Sciences, in press.

Grenestedt, J.L., 1998. Influence of wavy imperfections in cell walls on elastic stiffness of cellular solids. Journal of Mechanics and Physics of Solids 46, 29.

Gurson, A.L., 1977. Continuum theory of ductile rupture by void nucleation and growth: Part I — Yield criteria and flow rules for ductile porous media. Journal of Engineering Materials and Technology, 2.

Harte, A.-M., 1998. Private communication.

Harte, A.-M., Fleck, N.A., Ashby, M.F., 1999. Fatigue failure of an open cell and a closed cell aluminium alloy foam. Acta Metallurgica et Materialia 47 (8), 2511.

Hill, R., 1967. The essential structure of constitutive laws for metal composites and polycrystals. Journal of Mechanics and Physics of Solids 15, 79.

HKS, 1997. ABAQUS/Standard Users Manual, version 5.7. Hibbit, Karlsson and Sorensen Inc., Providence, Rhode Island.

Kraynik, A.M., Neilsen, M.K., Reinelt, D.A., Warren, W.E., 1997. Foam micromechanics. In: Proceedings of the NATO Advanced Study Institute on Foams, Emulsions and Cellular Materials, Cargese, Corsica.

Miller, R.E., 2000. A continuum plasticity model of the constitutive and indentation behaviour of foamed metals. International Journal of Mechanical Sciences, in press.

Silva, M.J., Hayes, W.C., Gibson, L.J., 1995. The effect of non-periodic microstructure on the elastic properties of two-dimensional cellular solids. International Journal of Mechanical Sciences 37, 1161.

Sugimura, Y., Rabiei, A., Evans, A.G., Harte, A.M., Fleck, N.A., 1998. Compression fatigue of a cellular Al alloy. Technical Report MECH 331. Division of Applied Sciences, Harvard University.

Triantafillou, T.C., Zhang, J., Shercliff, T.L., Gibson, L.J., Ashby, M.F., 1989. Failure surfaces for cellular materials under multiaxial loads-II: Comparison of models with experiment. International Journal of Mechanical Sciences 31, 665.

Zhang, J., Kikuchi, N., Li, V., Yee, A., Nusholtz, G., 1998. Constitutive modelling of polymeric foam material subjected to dynamic crash loading. International Journal of Impact Engineering 21 (5), 369.

Zhang, J., Lin, Z., Wong, A., Kikuchi, N., Li, V.C., Yee, A.F., Nusholtz, G.S., 1997. Constitutive modelling and material characterisation of polymeric foams. Journal of Engineering Materials and Technology (ASME) 119, 284.